 doi:10.20944/preprints202208.0108.v1

Article

Real-time Loosely Coupled 3DMA GNSS /Doppler Measurements Integration using a Graph Optimization and Its Performance Assessments in Urban Canyons of New York

Hoi-Fung Ng [1], Li-Ta Hsu [1,*], Max Jwo Lem Lee [1], Junchi Feng [2], Tahereh Naeimi [2], Mahya Beheshti [2], and John-Ross Rizzo [2]

[1] The Hong Kong Polytechnic University, Hong Kong; ivannhf.ng@connect.polyu.hk (H.-F.N.); lt.hsu@polyu.edu.hk (L.-T.H.); max.jl.lee@connect.polyu.hk (M.J.L.L)
[2] Grossman School of Medicine, New York University, New York 10016, United States; jf4151@nyu.edu (J.F.); taha.naeimi987@gmail.com (T.N.); beheshti.mahya@gmail.com (M.B.); johnrossrizzo@gmail.com (J.R.R)
* Correspondence: lt.hsu@polyu.edu.hk; Tel.: (optional; include country code; if there are multiple corresponding authors, add author initials)

Abstract: Smart health applications have received significant attention in recent years. Novel applications hold significant promise to overcome many of the inconveniences faced by persons with disabilities throughout daily living. For people with blindness and low vision (BLV), environmental perception is compromised, creating myriad difficulties. Precise localization is still a gap in the field and is critical to safe navigation. Conventional GNSS positioning cannot provide satisfactory performance in urban canyons. 3D mapping-aided (3DMA) GNSS may serve as an urban GNSS solution, since the availability of 3D city models has widely increased. As a result, this study developed a real-time 3DMA GNSS-positioning system based on state-of-the-art 3DMA GNSS algorithms. Shadow matching was integrated with likelihood-based ranging 3DMA GNSS, generating positioning hypothesis candidates. To increase robustness, the 3DMA GNSS solution was then optimized with Doppler measurements using factor graph optimization (FGO) in a loosely-coupled fashion. This study also evaluated positioning performance using an advanced wearable system's recorded data in New York City. The real-time forward processed FGO can provide a root-mean-square error (RMSE) with about 21 m. The RMSE drops to 16 m when the data is post-processed with FGO in a combined direction. Overall results show that the proposed loosely-coupled 3DMA FGO algorithm can provide a better and more robust positioning performance for the multi-sensor integration approach used by this wearable for persons with BLV.

Keywords: Localization; Navigation; Smartphone; GNSS; 3D Building Models

1. Introduction

Mobility and wayfinding are significant obstacles faced by people with BLV, specifically in urban areas. Degradation of the visual system can lead to a dramatic reduction in mobility. It has been shown that %80-%90 of people with BLV spend the majority of their time inside buildings, and %30 of them rarely leave home alone [1].

Accurate positioning is essential for the localization and navigation in the urban canyons. Pedestrians with BLV who live in urban areas could benefit significantly from an integrated navigation solution for use during activities of daily living. Much research has been performed to improve the autonomy of people with BLV, especially their ability to explore their environment. Rizzo et al. developed an advanced wearable in the form of an instrumented backpack equipped with microcomputers and sensors; this wearable incorporates cameras, IMUs, and GNSS positioning to provide a more comprehensive and full-featured navigation solution [3].

This study develops a real-time 3DMA GNSS-positioning system based on state-of-the-art 3DMA GNSS algorithms to advance the approach used for localization by the

Preprints (www.preprints.org) | NOT PEER-REVIEWED | Posted: 4 August 2022 doi:10.20944/preprints202208.0108.v1

wearable. The integration of shadow matching and likelihood-based ranging 3DMA GNSS methods were selected to evaluate positioning hypothesis candidates' likelihood scores.

Several experiments were designed in NYC to acquire GNSS data during urban commuting (travelling between two defined locations, origin and target). A commercial-grade receiver, u-blox ZED-F9P, was connected to an Nvidia microcomputer, Jetson TX2. The performance of the proposed system was evaluated with the data recorded in a series of trips that took place in the lower east side of NYC (specifically Murray Hill, Manhattan).

The remainder of this paper is organized as follows: section 2 will be an introduction to the integrated navigation system for pedestrians and existing studies. Section 3 will be an introduction to the proposed positioning algorithm. Section 4 is the designed experiment results and analysis. Finally, a conclusion and future work will be presented in section 5.

2. Navigation system for Visual impaired pedestrian

2.1. Overview of Navigation System for Visual Impaired Pedestrian

VIS^{4}ION (Visually Impaired Smart Service System for Spatial Intelligence and Navigation), is an advanced wearable consisting of a backpack with wide-angle high-resolution cameras on the support straps; these cameras with integrated microphones and IMUs are connected to a light-weight, portable computer for real-time analysis [1-8]. This wearable system may be used by the people with BLV during indoor and outdoor navigation, among other activities of daily living.

The platform provides real-time feedback using a binaural bone conduction headset and a haptic interface, allowing obstacle avoidance and situational awareness. More specifically, this mobile platform enables the users to understand their dynamically changing environment, giving them the agency to travel and wayfind independently. Our current **VIS^{4}ION** system can process 720p video at 10 fps (dependent on scene/task) and is robust without adding significant cognitive load to the end-user. This wearable runs off a laptop-battery with 66 Wh at 0.5 kg, yielding 3 hours of run-time function.

2.2. Importance of GNSS Positioning

Precise and reliable positioning is required to support safe navigation services for persons with BLV. GNSS provides continuous positioning in the global frame in absolute coordinates. However, the performance of GNSS navigation in the urban environment is unsatisfactory. GNSS signals can be blocked or reflected over buildings, resulting in the non-line-of-sight (NLOS) reception and multipath effect [9]. These errors become more severe in highly urban cities with many high-rise buildings, such as Hong Kong and New York. As a result, researchers are trying to improve positioning by integrating different aids, such as inertial measurement units (IMU) and cameras.

One of the most frequently used approaches to integrating the GNSS with IMU is pedestrian dead reckoning (PDR) [10]. The integration of GNSS and IMU takes advantage of two approaches. GNSS positioning can provide absolute coordinates in a global frame. However, the availability is limited by the number of visible satellites. The IMU can provide continuous positioning without subjection to external factors. However, it can only offer relative incremental coordinates in the local frame. At the same time, IMUs suffer from a continuous bias that accumulates over time. As a result, GNSS/INS integration can provide a continuous positioning with absolute coordinates.

A camera is another popular aid for an integrated positioning system, where it can provide the receiver's orientation in the local frame. Visual odometry (VO) [11] can extract the features from the image and estimate the relative orientation change of the receiver. VO assumes that feature points are static. Matching two consecutive frames can aid positioning by providing relative position. However, it is sensitive to illumination conditions and feature availability. Meanwhile, VO assumes the feature points are static, and therefore dynamic objects highly affect performance. When the feature points move in parallel

Preprints (www.preprints.org) | NOT PEER-REVIEWED | Posted: 4 August 2022 doi:10.20944/preprints202208.0108.v1

with the camera, the system may think it remains static itself. Therefore, research on tightly coupled VO with INS improves positioning performance [12].

Research also suggests using a sky-pointing fisheye camera to detect the NLOS signal via image recognition algorithms [13, 14]. Therefore, only the predicted healthy satellites are utilized for GNSS positioning. The limitation of excluding unhealthy satellites is that when many high-rise buildings surround the receiver, exclusion can result in bad satellite geometry and degrading performance.

Besides the aid of external sensors, improving the positioning accuracy of GNSS itself can definitely benefit the whole positioning system. Therefore, researchers are trying to identify and mitigate the NLOS error to improve the GNSS positioning alone. The consistency-check method [15] can detect and isolate unhealthy measurements and positioning performance can be improved to a satisfactory level. However, a consistency check will fail if the unhealthy measurements dominate the healthy ones [16].

Dual-frequencies measurements also demonstrate good performance in mitigating the multipath effects and isolating NLOS errors. Researchers use the nature of the higher resolution of L5-band measurements and design a new weighting scheme; the weighted least squares performance has been demonstrated to improve [17].

2.3. Related works on 3DMA GNSS

One popular approach to improve GNSS positioning in urban canyons is using a 3D building model to identify and even correct the NLOS reception error. 3D building models demonstrate a massive improvement for positioning, namely 3D mapping-aided (3DMA) GNSS [18]. An existing study uses the 3D building model to exclude the NLOS satellites; the weighted least squares (WLS) solution can therefore be enhanced [19]. However, we have to know the exact position to give a correct prediction and correction. As a result, the solution is usually determined as a particle-based approach. Position hypothesis candidates are distributed and measurements are modelled as the prediction at each candidate. The candidate with the highest similarity between modelled and actual received measurements is assumed to be the receiver location. Two basic categories of 3DMA GNSS algorithms are shadow matching and ranging-based 3DMA GNSS.

Shadow matching [20, 21] matches the satellite visibility at different locations. The received satellites are assumed to be the LOS, while the non-received ones are assumed to be NLOS. The ephemeris provides the satellites' position and matches the visibility at each candidate to find the highest visibility similarity.

Another 3DMA GNSS is the ranging-based method. The receiver location is determined by comparing the modelled and received pseudorange. Pseudorange measurements are modelled at each candidate. For the NLOS predicted satellite, the NLOS reflection delay is also modelled based on a geometrical or statistical approach. The absolute position of the reflecting point has to be determined for the geometrical approach. A popular approach is ray-tracing [22, 23]. It tests and validates the reflection path over each potential reflector, creating a high computational load. Therefore, an effective computational version called skymask 3DMA GNSS [24] was introduced. It determines the reflecting point over an enhanced skymask. The statistical approach, also known as likelihood-based ranging [25], uses a skew-normal distribution to model the NLOS delay measurements then remaps the errors to the LOS one with the normal distribution.

Performance of shadow matching and ranging-based 3DMA GNSS are different due to the healthy satellite and building geometry distribution. Shadow matching usually outperforms in the across-street direction, while ranging-based 3DMA GNSS obtains higher accuracy in the along-street direction. The complementary nature of the two approaches inspired researchers to integrate them. The latest study shows that an integrated solution of 3DMA GNSS can provide positioning accuracy of around 10 m or less in urban canyons with both single frequency [25] and multi-frequency [26] measurements.

However, most of these approaches only concern positioning in a single epoch. Hence the performance is not robust for continuous positioning. As a result, a temporal

Preprints (www.preprints.org) | NOT PEER-REVIEWED | Posted: 4 August 2022 doi:10.20944/preprints202208.0108.v1

connection is required to improve the reliability of urban GNSS positioning. There is research using the Kalman filter (KF) and extended Kalman filter (EKF) to recursively update the recent state through the prediction based on past estimation and error of current measurements [27, 28]. Researchers also use particle filters to effectively distribute and sample the candidates [29, 30]. Moreover, a grid filter was adopted to distribute positioning candidates evenly [25]. The filtering techniques demonstrate an excellent result in improving the smoothness of the positioning solution. Meanwhile, a machine learning approach can intelligently predict the change of signal status and estimate the most likely path on the map as the optimized positioning estimation [31].

Another approach is using factor graph optimization (FGO) [32], which optimizes the states of all epochs with many constraints. The solution will be highly robust as FGO optimizes all temporal constraints as a batch approach. Researchers open-sourced the FGO code that integrates GNSS positioning with Doppler measurements to provide a multi-epoch optimized solution [33]. FGO also applies to centimeter-level accuracy positioning via carrier-phase measurements, such as GNSS PPP [34] and RTK [33]. Furthermore, 3DMA GNSS-based collaborative positioning can benefit from FGO [35].

Different research demonstrates that FGO can provide an excellent positioning performance. This study will integrate 3DMA GNSS with velocity estimated by Doppler measurements as a loosely-coupled solution, and states are optimized via FGO. The integrated solution can provide a more robust trajectory for pedestrian applications, such as this wearable.

3. Proposed Real-Time 3D Mapping-Aided (3DMA) GNSS Positioning System

This section will introduce the proposed loosely-coupled 3DMA GNSS and velocity positioning system via FGO. The flowchart is shown in Figure 1.

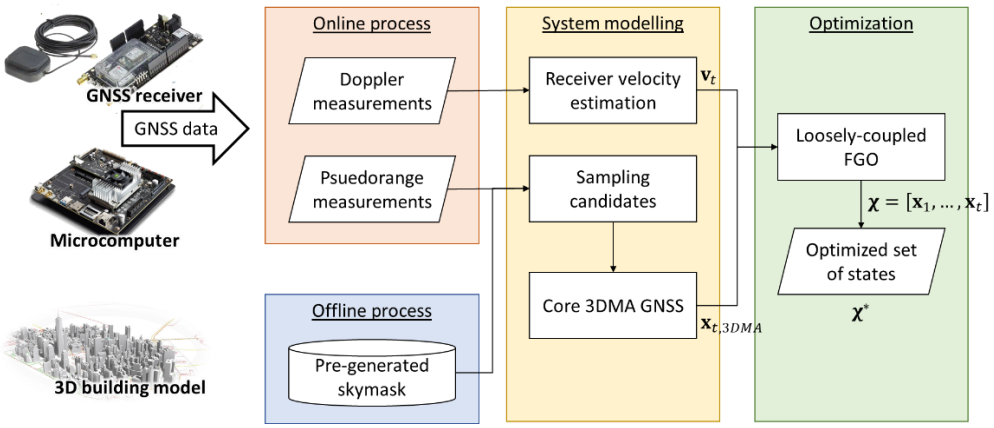

Figure 1. System flowchart on the proposed system.

3.1. Open-Sourced 3D City Models

3D models of New York City (NYC) were obtained from open-sourced repositories released by the Department of Information Technology & Telecommunications' (DoITT) 2014 aerial survey [36] with a level of detail (LoD) 2. The city model was registered to cartesian New York Long Island State Plane FIPS 3104 coordinates. The city model is shown in Figure 2.

Preprints (www.preprints.org) | NOT PEER-REVIEWED | Posted: 4 August 2022 doi:10.20944/preprints202208.0108.v1

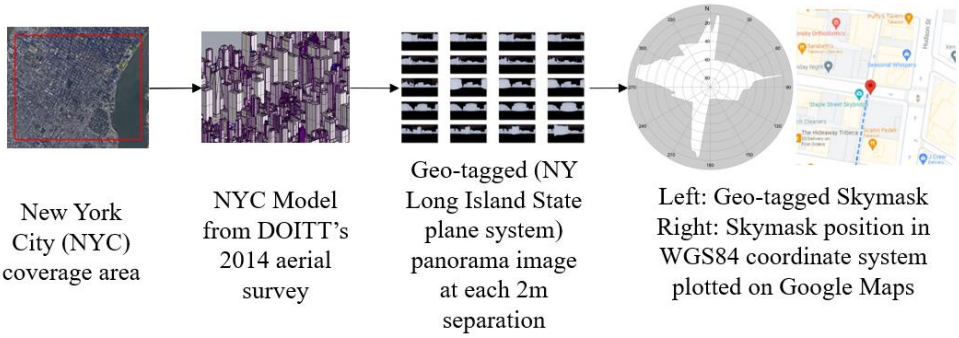

Figure 2. Geo-tagged skymask generation from NYC 3D model.

3.2. Offline Stage Skymasks Generation

A skymask is a skyplot with building boundaries for a single location. It is an array with a total of 360 entries that represents the azimuth angle from 0° to 359°. Each entry stores the highest elevation angle of the building blockage in degrees in the corresponding entry (each azimuth angle). Skymasks are generated in an offline stage. The intentional coverage area for the 3DMA GNSS was first selected, and then the 3D city models were downloaded. The models were imported into the Rhino 7 3D modelling software [37], and then converted to the Unreal engine-supported format for automated skymask generation [38]. The selected area was separated into 4 m catchments areas for each potential location to capture a 360° equirectangular image of the building outline. The skymask generation process is then performed by setting up a virtual camera in the Unreal engine to capture the panorama image at each potential location outside the building and above the terrain. Saved panorama images are then classified into obstacles and sky. At the cutting edge between obstacles and the sky, pixels are converted to angular position (azimuth and elevation angle) at the skymask. Lastly, each skymask corresponds to one position in the state plane coordinate system, which was converted to WGS84 for real-time 3DMA GNSS positioning. The extracted skymask at each available location was then saved to a specified format for the microcomputer to use during real-time positioning [24].

3.3. 3DMA GNSS Positioning Algorithm

3DMA GNSS evenly distributes the hypothesis positioning candidates during the online stage around the initial position. After that, the simulated measurements are generated to be compared with the received measurements for each candidate. Due to their computational efficiency, this study integrates shadow matching and likelihood-based ranging 3DMA GNSS. The implementation can be found in [26].

3.3.1. Skymask Context-based Candidates Sampling

An effective hypothesis positioning candidates sampling is important for 3DMA GNSS. The sampling area must cover the receiver location to achieve the theoretically best performance. Enlarging the sampling radius ensures the receiver location is being covered. However, this creates a massive computational load for the low-end microcomputer, which is not practical for a real-time application. Required computational time is proportional to the number of sampled candidates and received satellites. The computational time is within the necessary output rate. Thus, we proposed to use the surrounding skymasks and principal component analysis (PCA) to determine the street direction and distribute the sampling candidates effectively.

Candidate distribution is based on the weighted least squares (WLS) for the first epoch and using the previous epoch FGO solution as the initial position after it is available. An initial circle with a sampling radius, R, e.g. 50 m, is set up empirically to estimate the surrounding environment by weighted averaging skymask, $\overline{\mathbf{SM}}^{az}$.

Preprints (www.preprints.org) | NOT PEER-REVIEWED | Posted: 4 August 2022 doi:10.20944/preprints202208.0108.v1

$$\overline{\mathbf{SM}}^{az} = \frac{1}{\sum w_k}\sum_{k=1}^{K} w_k \mathbf{SM}_{\mathbf{P}_k}^{az} \quad \text{where } \mathbf{P}_k \in \{|\mathbf{P} - \mathbf{x}_{init}| < R\} \tag{1}$$

where $\mathbf{SM}_{P_k}^{az}$ is the skymask of location $\mathbf{P}_k$ where it is within the sampling radius R based on the initial location, $\mathbf{x}_{init}$. az is the array index represents the azimuth angle from 0° to 359°. $w_k = |\mathbf{P}_k - \mathbf{x}_{init}|^2$ is the weighting of location $\mathbf{P}_k$ based on the distance between the initial location, $\mathbf{x}_{init}$.

The averaged skymask is then converted to vectors in the Earth-Centered-Earth-Fixed (ECEF) frame together with the transformation matrix, $\mathbf{R}$, expressed as,

$$\mathbf{q}^{az} = \mathbf{R} \cdot [\sin az \cdot \cos \overline{\mathbf{SM}}^{az}, \cos az \cos \overline{\mathbf{SM}}^{az}] \tag{2}$$

where $\mathbf{R}$ is the transformation matrix that converts the vector in local frame to world frame in ECEF. Thus, we can form the variance-covariance matrix, $\mathbf{Q}$,

$$\mathbf{Q} = \mathbf{q}^{\mathrm{T}}\mathbf{q} \tag{3}$$

Therefore, we can obtain the eigenvalues, $\boldsymbol{\lambda} = \begin{bmatrix} \lambda_1 & 0 \\ 0 & \lambda_2 \end{bmatrix}$, and eigenvectors, $\mathbf{V} = [\mathbf{v}_1 \quad \mathbf{v}_2]$, from the variance-covariance matrix, $\mathbf{Q}$. Noted that the eigenvalues and eigenvectors are sorted in descending order, e.g. λ_1 and $\mathbf{v}_1$ denotes the they are with the largest eigenvalue. And the eigenvector with a larger eigenvalue can be interpreted as the street's longitudinal direction.

Finally, we can filter the initial circle with the ellipsoid based on determined eigenvalues and eigenvectors. Where the length of the semi-major and semi-minor axis are R and $R \cdot {\lambda_2}/{\lambda_1}$, respectively. And the direction of the semi-major and semi-minor axis are $\mathbf{v}_1$ and $\mathbf{v}_2$, respectively.

$$\mathbf{p}_{j=1\ldots J} = \left\{ \mathbf{P}_k \in \frac{(\mathbf{d}_k \cdot \mathbf{v}_1)^2}{R^2} + \frac{(\mathbf{d}_k \cdot \mathbf{v}_2)^2}{\left(R \cdot {\lambda_2}/{\lambda_1}\right)^2} < 1 \right\} \tag{4}$$

where $\mathbf{d}_k = \mathbf{P}_k - \mathbf{x}_{init}$ is the vector between the candidate's position, $\mathbf{P}_k$, and initial location, $\mathbf{x}_{init}$.

The distributed candidates are an ellipsoid with a semi-major axis of 50 m. The separation for each candidate is 4 m. The above settings are determined empirically and suitable for real-time processing on a low-end microcomputer used in this study. A semi-major axis of 50 m can cover the position error of the initial position in most cases. In comparison, separation with 4 m can reduce the number of distributed candidates while maintaining an acceptable accuracy level.

The proposed distribution can effectively distribute the hypothesis position candidates based on the surrounding environment. Figure 3 shows two typical cases in urban canyons. In road intersections, two eigenvalues are nearly the same (figure 3(b)), such that the candidates' distribution is almost a circle that covers the whole intersection, as shown in figure 3(a). In contrast, when the initial location is in a straight street, the largest eigenvalue is much larger than the other (figure 3(d)). The candidates are most likely distributed on the same street but not the next block.

Preprints (www.preprints.org) | NOT PEER-REVIEWED | Posted: 4 August 2022 doi:10.20944/preprints202208.0108.v1

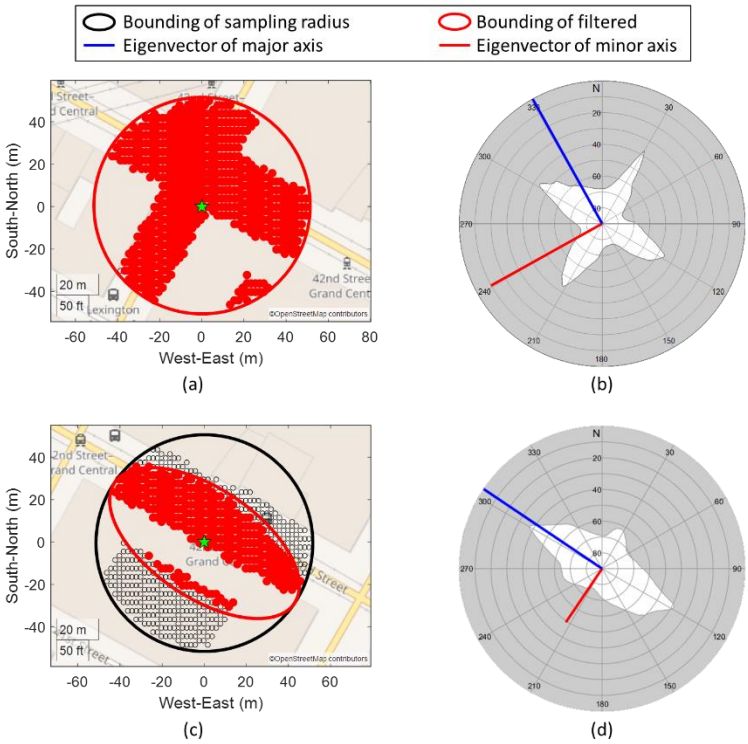

Figure 3. Typical cases on candidate sampling in urban environments on intersection ((a) and (b)) and straight street ((c) and (d)). Note that the eigenvectors (red and blue lines in (b) and (d)) are projected back to azimuth and elevation angle (local frame) for illustration here.

The prevention of candidate distribution at the next block can potentially mitigate the local minima issue caused by the high similarity of building geometry, as shown in Figure 4. Local minima are located on the next street (the high score part in red near the upper right corner). After applying the proposed skymask context-based candidates sampling strategy, the local minima issue can be mitigated.

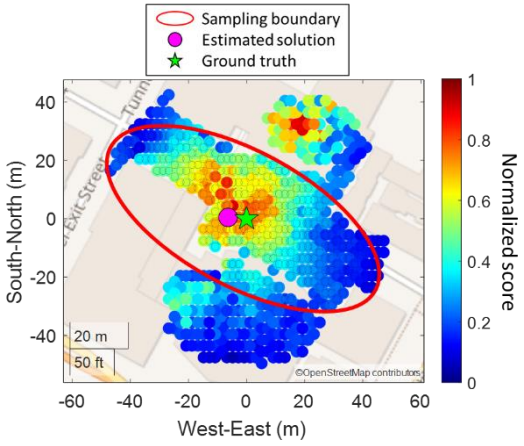

Figure 4. Example on skymask context-based candidates sampling.

To conclude, the skymask context-based candidates sampling can effectively distribute the position candidates. It has two main advantages. The first is to reduce the computational load by reducing the number of distributed candidates based on the surrounding environment. The second advantage is that candidates are most likely distributed on the same street. Therefore, the local minima on the next street can potentially be excluded.

Preprints (www.preprints.org) | NOT PEER-REVIEWED | Posted: 4 August 2022 doi:10.20944/preprints202208.0108.v1

3.3.2. Integrated solution of 3DMA GNSS

For each candidate $\mathbf{p}_{j=1\ldots J}$, the integrated likelihood score, $S_{j,SDM+LBR}$, will be evaluated,

$$S_{j,SDM+LBR} = \sqrt{S_{j,\mathrm{LBR}} \times S_{j,\mathrm{SDM}}} \tag{5}$$

where $S_{j,\mathrm{LBR}}$ and $S_{j,\mathrm{SDM}}$ are the likelihood score of likelihood-based ranging 3DMA GNSS and shadow matching, respectively. The detail of the calculation of the likelihood scores can be found at [26].

Shadow matching evaluates the visibility consistency between the measured carrier-to-noise-ratio (C/N_0) and prediction with skymask. Shadow matching requires all satellites in ephemerides to predict the non-received one. In implementation-wise, we automatically download ephemerides from the day prior. And it uses the same receiving time but a day before to estimate the satellite's angular position for visibility prediction with skymask. Suppose the internet is enabled for the execution platform. In that case, this can be replaced by assisted GNSS (AGNSS) [39, 40] and provide the satellite data to determine their position via standard protocol, such as secure user plane location (SUPL). This is easier to be achieved with built-in AGNSS devices, such as smartphones [41].

While likelihood-based ranging 3DMA GNSS, we model the pseudorange at each candidate position and compare it with the received pseudorange measurements. The NLOS predicted satellite at a candidate, likelihood-based ranging 3DMA GNSS remaps NLOS pseudorange difference to a LOS one using the distribution model.

The integrated solution of 3DMA GNSS, $\mathbf{x}_{\mathrm{3DMA}}$, is calculated by weighted averaging the distributed candidates with their likelihood score,

$$\mathbf{x}_{\mathrm{3DMA}} = \frac{\sum_{j=1}^{J} \mathbf{p}_j S_{j,SDM+LBR}}{\sum_{j=1}^{J} S_{j,SDM+LBR}} \tag{6}$$

The receiver location is then optimized via FGO as a loosely- coupled solution.

3.4. Loosely-Coupled Factor Graph Optimization (LC-FGO)

This study also optimized the 3DMA GNSS solution as a batch via forming the graphical optimization. It is associated with FGO, connecting two consecutive epochs' solutions with velocity. The overall structure of the FGO process is shown in Figure 5.

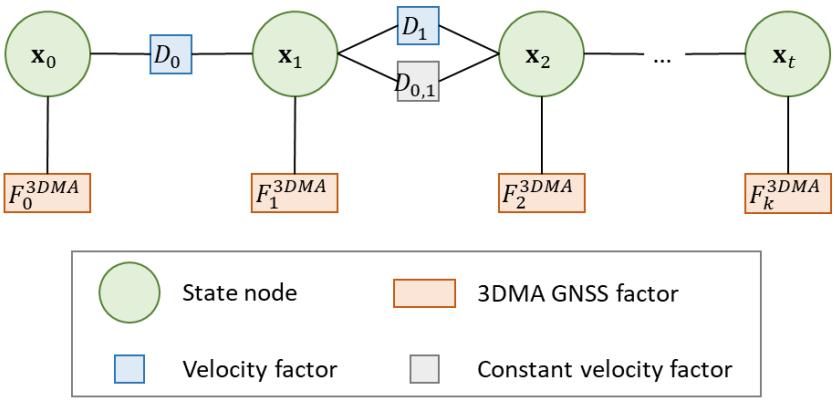

Figure 5. Structure of the proposed loosely-coupled 3DMA GNSS and velocity via FGO.

The error factor between the 3DMA GNSS solution, $\mathbf{x}_{t,3DMA}$, and optimized state, $\mathbf{x}_t$, is given by,

$$\left\| e_{t,\mathbf{3DMA}} \right\|^2_{\boldsymbol{\sigma}^2_{\mathbf{3DMA}}} = \left\| \mathbf{x}_t - \mathbf{x}_{t,3DMA} \right\|^2_{\boldsymbol{\sigma}^2_{\mathbf{3DMA}}} \tag{7}$$

Preprints (www.preprints.org) | NOT PEER-REVIEWED | Posted: 4 August 2022 doi:10.20944/preprints202208.0108.v1

where $\boldsymbol{\sigma}^2_{\mathbf{3DMA}} = \alpha \cdot \mathrm{diag}\left(\left[\sigma^2_{3DMA,x}, \sigma^2_{3DMA,y}, \sigma^2_{3DMA,z}\right]\right)$ is a diagonal variance matrix of the 3DMA GNSS. Constant $\alpha = 1$ is an empirically determined tuning factor for 3DMA GNSS error factor. Variance at each axis is taken by the distance variation between the 3DMA GNSS solution and candidates with the highest 10% likelihood score, divided by the separation of candidates, γ,

$$\boldsymbol{\sigma}^2_{\mathbf{3DMA}} = \frac{1}{\gamma}\mathrm{Var}\left(\left|\mathbf{x}_{t,3DMA} - \mathbf{x}_{t,10\%}\right|\right) \tag{8}$$

where $\mathbf{x}_{t,10\%}$ represents the candidates' position with the highest 10% likelihood score. $|\cdot|$ denotes the Euclidean distance between two positions.

Receiver velocity, $\mathbf{v}_t$, and clock drift, $c\dot{\delta}t_t$, is estimated by the Doppler measurements of every satellite i at epoch t, $d_t = \left[d_t^1, \ldots, d_t^i\right]$, via the least-squares (LS) method [33]. The error factor between consecutive epochs can be expressed as follows,

$$\left\|e_{t,\mathbf{v}}\right\|^2_{\boldsymbol{\sigma}^2_{\mathbf{v},t}} = \left\|\mathbf{v}_t - \frac{1}{\Delta t}(\mathbf{x}_{t+1} - \mathbf{x}_t)\right\|^2_{\boldsymbol{\sigma}^2_{\mathbf{v},t}} \tag{9}$$

where Δt is the time difference between epoch t and $t+1$. $\boldsymbol{\sigma}^2_{\mathbf{v}} = \beta \cdot \mathrm{diag}\left(\left[\sigma^2_{v,x}, \sigma^2_{v,y}, \sigma^2_{v,z}\right]\right)$ is a diagonal covariance matrix associated with the velocity $\mathbf{v}_t$ at x-, y-, and z-axis, respectively. And constant $\beta = 5.2$ is an empirically determined tuning factor for velocity error factor.

A constant velocity motion model [42] is included in this graph structure to provide a smoothed trajectory estimation. As this study assumed, users' motions are small with an ignorable acceleration. This factor minimizes the error between the position change between two epochs and the averaged velocity estimated via Doppler measurements, modelled as follows,

$$\left\|e_{t,\bar{\mathbf{v}}}\right\|^2_{\boldsymbol{\sigma}^2_{\bar{\mathbf{v}}}} = \left\|\frac{1}{2}(\mathbf{v}_t + \mathbf{v}_{t+1}) - \frac{1}{\Delta t}(\mathbf{x}_{t+1} - \mathbf{x}_t)\right\|^2_{\boldsymbol{\sigma}^2_{\bar{\mathbf{v}}}} \tag{10}$$

where $\boldsymbol{\sigma}^2_{\bar{\mathbf{v}}} = \frac{1}{2}\left(\boldsymbol{\sigma}^2_{\mathbf{v},t} + \boldsymbol{\sigma}^2_{\mathbf{v},t+1}\right)$ is the averaged diagonal covariance matrix at time t and $t+1$.

The cost function for the position estimation of the proposed loosely-coupled 3DMA GNSS via FGO is formulated as,

$$\boldsymbol{\chi}^* = \underset{\boldsymbol{\chi}}{\mathrm{argmin}} \sum_k \left\|e_{t,\mathbf{3DMA}}\right\|^2_{\boldsymbol{\sigma}^2_{\mathbf{3DMA}}} + \left\|e_{t,\mathbf{v}}\right\|^2_{\boldsymbol{\sigma}^2_{\mathbf{v},t}} + \left\|e_{t,\bar{\mathbf{v}}}\right\|^2_{\boldsymbol{\sigma}^2_{\bar{\mathbf{v}}}} \tag{11}$$

where $\boldsymbol{\chi} = [\mathbf{x}_1, \ldots, \mathbf{x}_t]$ is the state set of the receiver. And $\boldsymbol{\chi}^*$ denotes the optimal states set. For computational efficiency, a sliding window for FGO is set as 200 s, which is determined empirically.

4. Experiments and Results

4.1. Experiment Setup

A commercial-grade receiver, u-blox ZED-F9P, was connected to a microcomputer, Nvidia Jetson TX2. A total of four satellite constellations with a single frequency were enabled during the experiments: GPS L1, GLONASS G1, Galileo E1, and Beidou B1. We modified the open-source library RTKLIB [43] for the GNSS-related processes. Google Ceres Solver [44] was used for the NLS and FGO processes. Several experiments took place in the lower east side of NYC (Murray Hill, Manhattan (zip code 10016)). In these experiments, 2 team members walked fixed navigation routes as if commuting between an origin (NYU Medical Center) and specific target destinations (storefronts) in a 1-mile radius. A total of 11 trips were made and used for analysis.

The ground truth reference trajectory was obtained via post-processing. The pedestrian subjects who collected the data walked straight lines and made the best attempts not to veer. Starting and ending locations and locations in between were labelled manually. We also equipped a smartphone during the experiment and recorded the device location

Preprints (www.preprints.org) | NOT PEER-REVIEWED | Posted: 4 August 2022 doi:10.20944/preprints202208.0108.v1

output. And we use the smartphone output location to interpolate the longitudinal speed and project the vector between starting and ending location.

4.2. Experiment Results

The evaluation was aimed at comparing the proposed algorithms in both a real-time and post-processing manner, also with several conventional solutions:

1. **WLS**: weighted least squares method [43], uses pseudorange to estimate receiver location.
2. **3DMA GNSS**: snapshot state-of-the-art 3DMA GNSS with positioning hypothesis candidates [26].
3. **LC-FGO (proposed)**: real-time forward (instantaneous) processed loosely-coupled FGO solution with integrated 3DMA GNSS and velocity.
4. **LC-FGO-PP (proposed)**: combined (forward and backward) processed loosely-coupled FGO solution with integrated 3DMA GNSS and velocity.

The optimization frame was under the ECEF coordinate system. The comparison is divided into root-mean-squared error (RMSE) and standard deviation (STD) positioning error in meters.

A total of 11 experimental navigation trips were done in New York City, the positioning results of different trips are shown in Table 1. In summary, the candidate-based 3DMA GNSS always outperforms the conventional WLS. After integrating the velocity and optimizing it only forward direction, the positioning accuracy is improved. If constraints optimization is performed in a combined manner, the positioning accuracy becomes higher. Overall performance of different experiments, the RMSE and STD of 3DMA GNSS are 25.34 m and 19.46 m, respectively. At the same time, LC-FGO is 21.05 m and 14.60 m for RMSE and STD, respectively. LC-FGO-PP have a stronger constraint between epochs and obtains RMSE of 15.97 m while STD is 12.48 m. Two FGO have a smaller RMSE, which means that the overall performance is better than that of 3DMA GNSS, and a lower STD implies that they are more robust. And we selected two trips out of eleven (one good and bad case, respectively) to further discuss in this section.

Table 1. Statistics on positioning results of all experiments

Navigation trips	Epochs (s)	Algorithm	RMSE (m)	STD (m)
1	952	1. WLS	38.30	20.00
		2. 3DMA GNSS	19.70	15.51
		3. LC-FGO	24.66	14.95
		4. LC-FGO-PP	15.54	12.25
2	979	1. WLS	59.15	26.94
		2. 3DMA GNSS	29.14	16.75
		3. LC-FGO	33.56	17.13
		4. LC-FGO-PP	24.66	13.08
3	574	1. WLS	62.66	38.62
		2. 3DMA GNSS	27.62	16.40
		3. LC-FGO	22.98	11.04
		4. LC-FGO-PP	21.38	9.51
4	607	1. WLS	91.98	54.99
		2. 3DMA GNSS	21.08	12.26
		3. LC-FGO	13.01	6.48

Preprints (www.preprints.org) | NOT PEER-REVIEWED | Posted: 4 August 2022 doi:10.20944/preprints202208.0108.v1

		4. LC-FGO-PP	14.09	6.85
5	599	1. WLS	30.34	10.46
		2. 3DMA GNSS	22.64	13.21
		3. LC-FGO	20.38	10.25
		4. LC-FGO-PP	18.90	11.18
6	934	1. WLS	39.17	19.54
		2. 3DMA GNSS	18.27	11.28
		3. LC-FGO	15.32	10.44
		4. LC-FGO-PP	14.56	8.73
7	885	1. WLS	44.25	25.89
		2. 3DMA GNSS	18.64	11.27
		3. LC-FGO	25.17	11.03
		4. LC-FGO-PP	12.17	6.08
8	513	1. WLS	36.43	15.94
		2. 3DMA GNSS	16.55	9.46
		3. LC-FGO	21.30	8.36
		4. LC-FGO-PP	14.22	7.47
9	878	1. WLS	40.86	21.21
		2. 3DMA GNSS	41.50	26.91
		3. LC-FGO	44.62	29.99
		4. LC-FGO-PP	37.67	24.91
10	742	1. WLS	49.43	31.11
		2. 3DMA GNSS	26.72	15.29
		3. LC-FGO	25.49	13.08
		4. LC-FGO-PP	20.46	11.15
11	733	1. WLS	62.33	37.96
		2. 3DMA GNSS	36.85	28.13
		3. LC-FGO	37.82	27.85
		4. LC-FGO-PP	32.13	26.08

We first present a trip with a good positioning performance (Trip 6). It starts from a relative open-sky area and walks along straight to a deep urban canyon. The plots are shown in Figure 6.

Preprints (www.preprints.org) | NOT PEER-REVIEWED | Posted: 4 August 2022 doi:10.20944/preprints202208.0108.v1

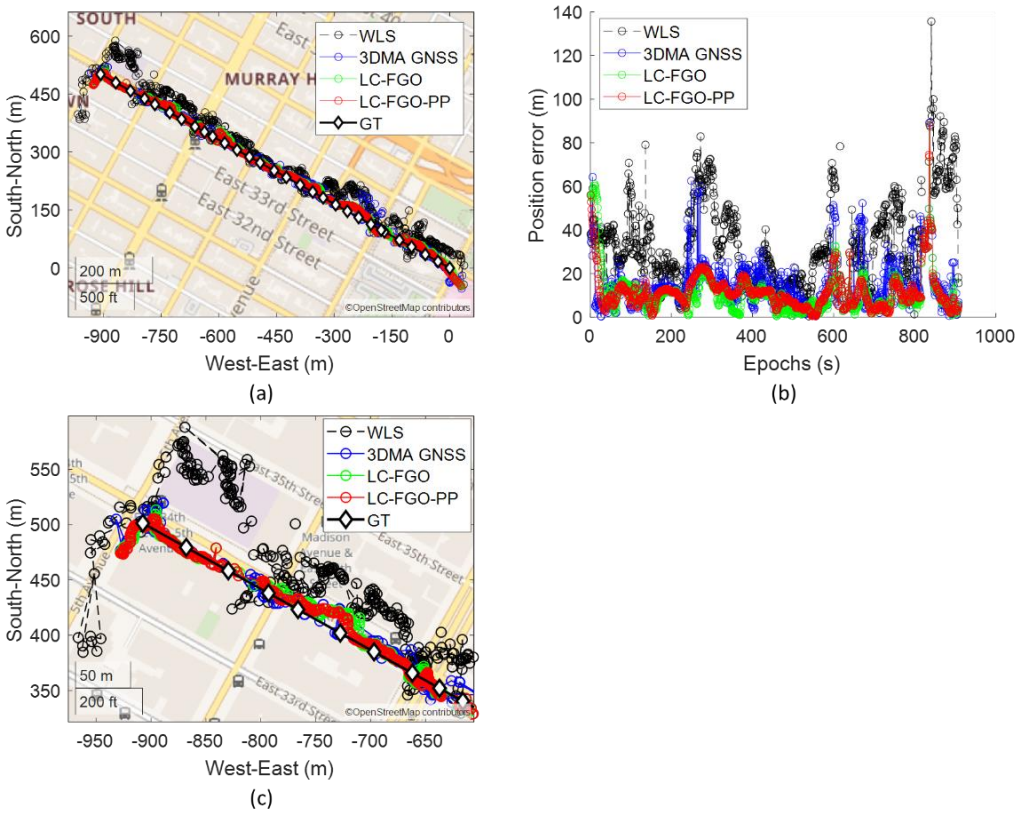

Figure 6. (a) map plot, (b) positioning errors, and (c) magnified map plot of last 300 epochs of good positioning trip.

In this experiment, it can be observed that the 3DMA GNSS outperforms WLS by twofold, and the positioning RMSE are 18.27 m and 39.17 m, respectively. Many solutions for WLS located on the opposite side or on the wrong street, as shown in 6(c). With the aid of 3D models, 3DMA can correct the solution back to the correct street. If further integrated with the Doppler measurements, the positioning error can be suppressed in most cases, especially around epochs 200 s to 600 s. Results in the RMSE of the forward LC-FGO and combined FGO (LC-FGO-PP) are 15.32 m and 14.56 m, respectively.

Followed by a navigation trip with bad positioning results (Trip 2). It begins in a deep urban canyon and walks along the street to a relatively open area which is opposite to Experiment 6. The map and error plot of this experiment are shown in Figure 7.

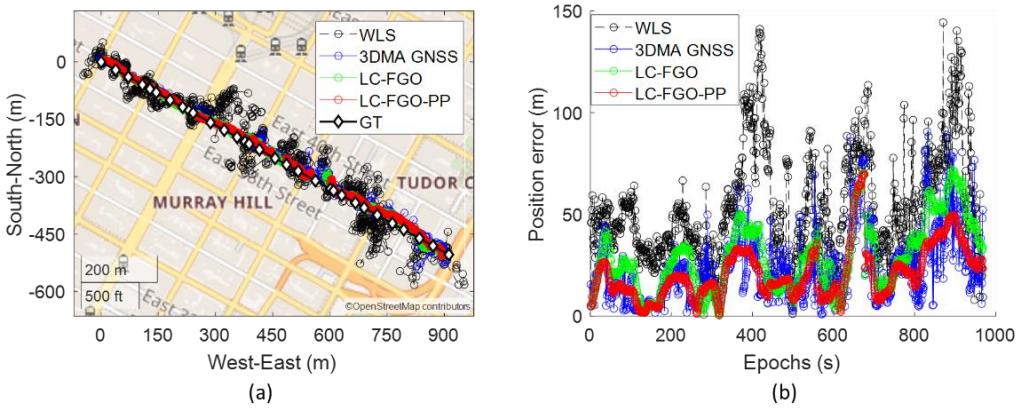

Figure 7. (a) map plot and (b) positioning errors of experiment 2.

Preprints (www.preprints.org) | NOT PEER-REVIEWED | Posted: 4 August 2022 doi:10.20944/preprints202208.0108.v1

Similar to Experiment 6, both 3DMA GNSS and two LC-FGO algorithms outperform WLS. The RMSE of WLS, 3DMA GNSS, LC-FGO, and LC-FGO-PP are 59.15 m, 29.14 m, 33.56 m, and 24.66 m, respectively. However, the LC-FGO is not outperforming the 3DMA GNSS. The main error comes from the last 200 epochs. The performance of 3DMA GNSS keeps fluctuating during this period. And the natural difference between 3DMA GNSS and FGO results in the average performance of this experiment. 3DMA GNSS is a snapshot estimation, and each epoch performance is independent of the other. However, the FGO is different, especially for the forward FGO. The fluctuation of the 3DMA GNSS will keep accumulating errors in batch optimization. Therefore, the future estimation is affected. However, the combined FGO, LC-FGO-PP, has a much stronger constraint that tries to optimize the solution in both directions. As a result, the positioning error can be suppressed. Therefore, if the performance of LC-FGO has to be improved, marginalization analysis must be done to find the acceptable error of this graphical problem. And we must adaptively select the existing trustworthy information in the sliding window.

Near the end of the experiment, some 3DMA GNSS solutions wrongly estimate the position of the next block, as shown in Figure 8(a). The reason is that the receiver is located in a relatively open area. The PCA result of the average skymask indicates that the two eigenvalues are similar, and there is no clear major and minor axis. Results in the candidate distribute as a full circle, and the solution estimates at the local minima, as shown in Figure 8(b). The candidate might have to distribute based on the user's average historical motion to resolve this issue. However, a pedestrian's motion is not as consistent as a vehicle's, such distributing candidates based on average motion cannot capture a rapid motion change. Otherwise, an inertial measurement unit (IMU) has to be installed to detect instant motion change.

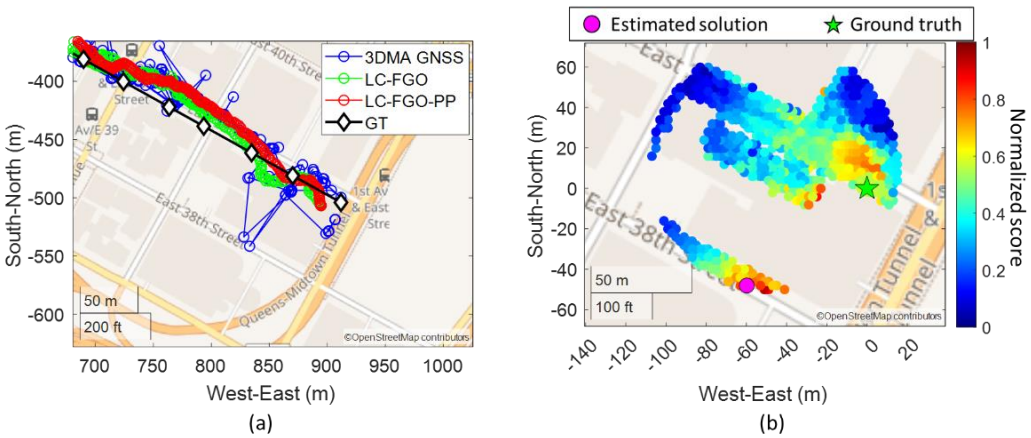

Figure 8. (a) zoom-in map plot near the end of experiment 2. (b) one of the epochs with large position error due to local minima problem.

Lastly, we also demonstrate a vehicle case in Hong Kong using the same receiver. The experiment covers different scenarios of an urban city, from open-sky areas to deep urban canyons. The data can be found in [45]. Positioning statistics are shown in Table 2, and the map plot and error plot are shown in Figure 9.

Preprints (www.preprints.org) | NOT PEER-REVIEWED | Posted: 4 August 2022 doi:10.20944/preprints202208.0108.v1

Table 2. Statistics of vehicle-mounted trip results.

Algorithm	RMSE (m)	STD (m)
1. WLS	14.92	9.20
2. 3DMA GNSS	7.94	4.85
3. LC-FGO	8.09	4.55
4. LC-FGO-PP	5.80	2.95

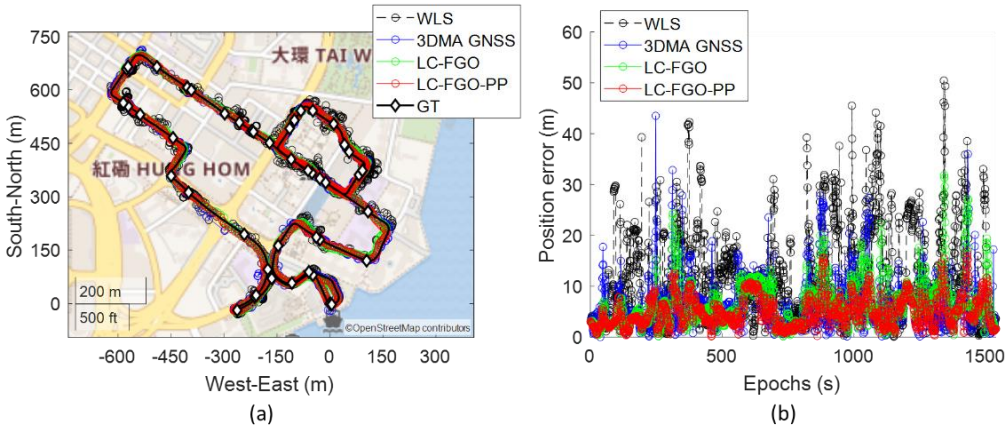

Figure 9. (a) map plot and (b) positioning errors of the vehicle-mounted experiment.

Both 3DMA GNSS and FGO outperform WLS in this case. RMSE of WLS, 3DMA GNSS, LC-FGO, and LC-FGO-PP are 14.92 m, 7.94 m, 8.09 m, and 5.80 m, respectively. Overall positioning outperformed that in New York. The excellent positioning performance has two main reasons. Firstly, the scenario of 11 trips in New York is more urbanized than that of the vehicle case in Hong Kong. The average skymasks' elevation angle at ground truths in all navigation trips is 58.6° and 46.9° for New York and Hong Kong, respectively. Secondly, measurement noise is suffered from the variation of the motion [46]. The vehicle case has higher dynamic motion, and measurements are less suffered from the multipath effects, better positioning performance can be obtained. We labelled the pseudorange error using the double differencing technique [47] for the good case in the New York dataset (Trip 6) and Hong Kong driving case, as shown in Figure 10. It can be observed that Hong Kong's dataset obtains a better pseudorange quality, and it is reasonable that a better positioning performance can be obtained in the Hong Kong vehicle data.

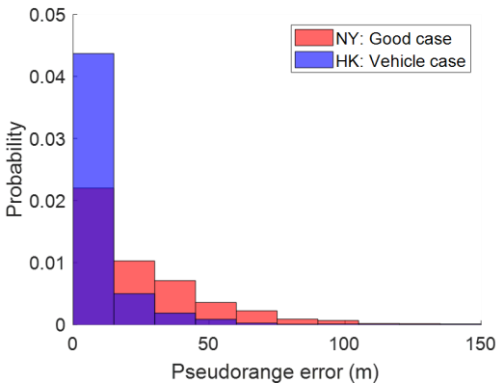

Figure 10. Probability density function plot on pseudorange error labelled by double differencing technique.

Preprints (www.preprints.org) | NOT PEER-REVIEWED | Posted: 4 August 2022 doi:10.20944/preprints202208.0108.v1

A similar conclusion can be made in this vehicle-mounted experiment based on the results. 3DMA GNSS and LC-FGO obtain similar performance in this data, but comparing the positioning error shown in Figure 9(b), LC-FGO can reduce the positioning better than the 3DMA, resulting in a smaller standard deviation on the positioning error. In other words, LC-FGO can provide a smoother and more robust trajectory, which applies to LC-FGO-PP. However, the error of velocity can degrade the integration performance. Figure 11 shows the epoch around 1300s. Although the 3DMA GNSS performs well, the wrong velocity estimated by Doppler measurements with WLS results in wrong integrated results. As a result, error mitigation or a correction for Doppler measurements have to be explored in the future. Also, tightly coupled with Doppler measurements can potentially address the problem. The wrong Doppler measurement can be identified and isolated from the state estimation separately. A sophisticated model can be developed to model the Doppler errors [48] so that inaccurate measurements can be used in the future.

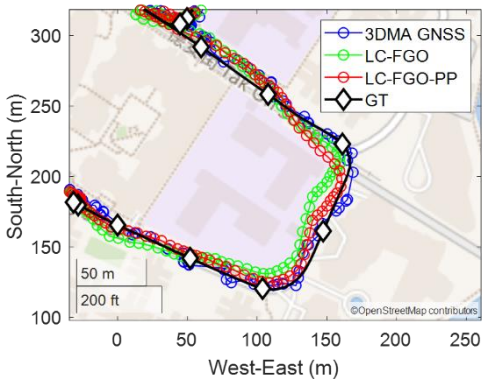

Figure 11. Zoom in map plot of positioning error caused by badly estimated velocity.

4.3. Computational Load and Storage Requirements

One of the main contributions of this study is to develop a real-time positioning system. Therefore, the processing time of a single epoch solution is important to guidance for a real-time operation that needs to maintain an output rate of 1 Hz. The computational load is directly proportional to the number of distributed candidates (sampling radius) and available satellites. From the result, the average number of visible satellites and sampled candidates are 26 and 1,143, respectively. The processing time for a single epoch solution is 0.91s. In other words, the implemented system can provide a real-time operation at a 1 Hz output rate.

Another important point for 3DMA GNSS implementation is the format employed to store the information of 3D building models. It is impossible for a microcomputer to generate skymask online or in real-time. Therefore, the skymask is pre-generated offline and stored in CSV format, as in [45]. If we were to cover the New York downtown area (around 3.6 km by 2.9 km), a total of 812,403 locations (outside the buildings) with 4 m separations for each candidate, the total file size of requisite skymasks would be 1.30 GB. This storage is still manageable for city-scoped applications. If the system has to be extended state-wise, further engineering work must be done to devise a sustainable solution for skymask database implementation.

5. Conclusions and Future Work

This study developed a real-time loosely-coupled 3DMA GNSS with Doppler measurements positioning system via FGO. And skymask context-based candidate sampling.

 doi:10.20944/preprints202208.0108.v1

Our approach distributes the candidates more effectively and mitigates local minima issues. Based on the experimental results, the positioning RMSE of loosely-coupled 3DMA GNSS with Doppler measurements via FGO is around 21 m with STD 15 m (on average). Performance can be further improved when optimizing in a combined direction with RMSE reduced to about 16 m with a STD of 13 m. The FGO can provide a lower standard deviation error than the candidate-based 3DMA GNSS, which means that it can provide a smoother and more robust solution.

However, the performance of LC-FGO still has space to be improved. The results show that candidate-based 3DMA GNSS intermittently outperforms LC-FGO. The reason is the positioning error of 3DMA GNSS keeps contributing to the integration with Doppler measurements. Accumulated error results affect future batch optimization. An adaptive scheme should be developed to select the high confidence information in the sliding window.

Furthermore, bad Doppler measurements result in wrong estimated velocity. This will degrade the FGO performance. Doppler measurements error mitigation or correction is the key to improving the positioning. In future steps, we will explore how 3DMA GNSS can more tightly integrate with Doppler measurements to provide a more robust positioning in the urban canyons for smart health applications and beyond.

Acknowledgments: Research reported in this publication was supported in part by the NSF grant 1952180 under the Smart and Connected Community program, the National Eye Institute of the National Institutes of Health under Award Number R21EY033689, and DoD grant VR200130 under the Delivering Sensory and Semantic Visual Information via Auditory Feedback on Mobile Technology" The content is solely the responsibility of the authors and does not necessarily represent the official views of the National Institutes of Health and NSF, and DoD.

References

1. Rizzo, J.-R.; Feng, C.; Riewpaiboon, W.; Mongkolwat, P. In *A Low-Vision Navigation Platform for Economies in Transition Countries*, 2020 IEEE World Congress on Services (SERVICES), 2020; IEEE: 2020; pp 1-3.
2. Niu, L.; Qian, C.; Rizzo, J.-R.; Hudson, T.; Li, Z.; Enright, S.; Sperling, E.; Conti, K.; Wong, E.; Fang, Y. In *A wearable assistive technology for the visually impaired with door knob detection and real-time feedback for hand-to-handle manipulation*, Proceedings of the IEEE International Conference on Computer Vision Workshops, 2017; 2017; pp 1500-1508.
3. Gui, W.; Li, B.; Yuan, S.; Rizzo, J.-R.; Sharma, L.; Feng, C.; Tzes, A.; Fang, Y. In *An assistive low-vision platform that augments spatial cognition through proprioceptive guidance: Point-to-Tell-and-Touch*, 2019 IEEE/RSJ International Conference on Intelligent Robots and Systems (IROS), 2019; IEEE: 2019; pp 3817-3822.
4. Boldini, A.; Garcia, A. L.; Sorrentino, M.; Beheshti, M.; Ogedegbe, O.; Fang, Y.; Porfiri, M.; Rizzo, J.-R., An inconspicuous, integrated electronic travel aid for visual impairment. *ASME Letters in Dynamic Systems and Control* **2021,** 1, (4).
5. Li, X.; Cui, H.; Rizzo, J.-R.; Wong, E.; Fang, Y. In *Cross-Safe: A computer vision-based approach to make all intersection-related pedestrian signals accessible for the visually impaired*, Science and Information Conference, 2019; Springer: 2019; pp 132-146.
6. Rizzo, J.-R.; Pan, Y.; Hudson, T.; Wong, E. K.; Fang, Y. In *Sensor fusion for ecologically valid obstacle identification: Building a comprehensive assistive technology platform for the visually impaired*, 2017 7th International Conference on Modeling, Simulation, and Applied Optimization (ICMSAO), 2017; IEEE: 2017; pp 1-5.
7. Shoureshi, R. A.; Rizzo, J. R.; Hudson, T. E. In *Smart wearable systems for enhanced monitoring and mobility*, Advances in Science and Technology, 2017; Trans Tech Publ: 2017; pp 172-178.
8. Phamduy, P.; Rizzo, J.-R.; Hudson, T. E.; Torre, M.; Levon, K.; Porfiri, M., Communicating through touch: Macro fiber composites for tactile stimulation on the abdomen. *IEEE transactions on haptics* **2017,** 11, (2), 174-184.
9. Groves, P. D., Multipath vs. NLOS signals. *Inside GNSS* **2013,** 8, 40-42.

10. Asano, S.; Wakuda, Y.; Koshizuka, N.; Sakamura, K. In *A robust pedestrian dead-reckoning positioning based on pedestrian behavior and sensor validity*, Proceedings of the 2012 IEEE/ION Position, Location and Navigation Symposium, 23-26 April 2012, 2012; 2012; pp 328-333.
11. Steinbrücker, F.; Sturm, J.; Cremers, D. In *Real-time visual odometry from dense RGB-D images*, 2011 IEEE International Conference on Computer Vision Workshops (ICCV Workshops), 6-13 Nov. 2011, 2011; 2011; pp 719-722.
12. Qin, T.; Li, P.; Shen, S., VINS-Mono: A Robust and Versatile Monocular Visual-Inertial State Estimator. *IEEE Transactions on Robotics* **2018,** 34, (4), 1004-1020.
13. Suzuki, T.; Kubo, N., N-LOS GNSS signal detection using fish-eye camera for vehicle navigation in urban environments. *27th International Technical Meeting of the Satellite Division of the Institute of Navigation, ION GNSS 2014* **2014,** 3, 1897-1906.
14. Moreau, J.; Ambellouis, S.; Ruichek, Y., Fisheye-Based Method for GPS Localization Improvement in Unknown Semi-Obstructed Areas. *Sensors* **2017,** 17, (1), 119.
15. Groves, P. D.; Jiang, Z., Height Aiding, C/N0 Weighting and Consistency Checking for GNSS NLOS and Multipath Mitigation in Urban Areas. *Journal of Navigation* **2013,** 66, (5), 653-669.
16. Hsu, L.-T.; Tokura, H.; Kubo, N.; Gu, Y.; Kamijo, S., Multiple Faulty GNSS Measurement Exclusion Based on Consistency Check in Urban Canyons. *IEEE Sensors Journal* **2017,** 17, (6), 1909-1917.
17. Ng, H.-F.; Zhang, G.; Yang, K.-Y.; Yang, S.-X.; Hsu, L.-T., Improved weighting scheme using consumer-level GNSS L5/E5a/B2a pseudorange measurements in the urban area. *Advances in Space Research* **2020,** 66, (7), 1647-1658.
18. Groves, P. D., It's Time for 3D Mapping–Aided GNSS. *Inside GNSS Magazine* **2016**, 50-56.
19. Obst, M.; Bauer, S.; Wanielik, G. In *Urban multipath detection and mitigation with dynamic 3D maps for reliable land vehicle localization*, Proceedings of the 2012 IEEE/ION Position, Location and Navigation Symposium, Myrtle Beach, SC, USA, 2012; Myrtle Beach, SC, USA, 2012; pp 685-691.
20. Wang, L.; Groves, P. D.; Ziebart, M. K., GNSS Shadow Matching: Improving Urban Positioning Accuracy Using a 3D City Model with Optimized Visibility Scoring Scheme. *NAVIGATION, Journal of the Institute of Navigation* **2013,** 60, (3), 195-207.
21. Wang, L.; Groves, P. D.; Ziebart, M. K., Smartphone Shadow Matching for Better Cross-street GNSS Positioning in Urban Environments. *Journal of Navigation* **2015,** 68, (3), 411-433.
22. Hsu, L.-T.; Gu, Y.; Kamijo, S., 3D building model-based pedestrian positioning method using GPS/GLONASS/QZSS and its reliability calculation. *GPS Solutions* **2016,** 20, (3), 413-428.
23. Miura, S.; Hsu, L.-T.; Chen, F.; Kamijo, S., GPS Error Correction With Pseudorange Evaluation Using Three-Dimensional Maps. *IEEE Transactions on Intelligent Transportation Systems* **2015,** 16, (6), 3104-3115.
24. Ng, H.-F.; Zhang, G.; Hsu, L.-T., A Computation Effective Range-based 3D Mapping Aided GNSS with NLOS Correction Method. *Journal of Navigation* **2020,** 73, (6), 1202-1222.
25. Zhong, Q.; Groves, P. D., Multi-Epoch 3D-Mapping-Aided Positioning using Bayesian Filtering Techniques. *NAVIGATION* 69.
26. Ng, H.-F.; Zhang, G.; Luo, Y.; Hsu, L.-T., Urban positioning: 3D mapping-aided GNSS using dual-frequency pseudorange measurements from smartphones. *NAVIGATION, Journal of the Institute of Navigation* **2021,** 68, (4), 727-749.
27. Groves, P. D., *Principles of GNSS, Inertial, and Multisensor Integrated Navigation Systems, Second Edition*. 2nd ed.; Artech House: 2013.
28. Zhang, G.; Wen, W.; Xu, B.; Hsu, L.-T., Extending Shadow Matching to Tightly-Coupled GNSS/INS Integration System. *IEEE Transactions on Vehicular Technology* **2020,** 69, (5), 4979-4991.
29. Yozevitch, R.; Moshe, B. B., A Robust Shadow Matching Algorithm for GNSS Positioning. *Navigation: Journal of The Institute of Navigation* **2015,** 62, (2), 95-109.
30. Suzuki, T. In *Integration of GNSS Positioning and 3D Map using Particle Filter*, Proceedings of the 29th International Technical Meeting of the Satellite Division of The Institute of Navigation (ION GNSS+ 2016), Portland, Oregon, 2016; Portland, Oregon, 2016; pp 1296-1304.

31. Ziedan, N. I. In *Optimized Position Estimation in Multipath Environments using Machine Learning*, Proceedings of the 34th International Technical Meeting of the Satellite Division of The Institute of Navigation (ION GNSS+ 2021), St. Louis, Missouri, 2021; St. Louis, Missouri, 2021; pp 3437-3451.
32. Sünderhauf, N.; Protzel, P. In *Towards robust graphical models for GNSS-based localization in urban environments*, International Multi-Conference on Systems, Signals & Devices, Chemnitz, Germany, 2012; Chemnitz, Germany, 2012; pp 1-6.
33. Wen, W.; Hsu, L.-T. In *Towards Robust GNSS Positioning and Real-time Kinematic Using Factor Graph Optimization*, 2021 IEEE International Conference on Robotics and Automation (ICRA), Xi'an, China, 2021; Xi'an, China, 2021; pp 5884-5890.
34. Watson, R. M.; Gross, J. N. In *Evaluation of Kinematic Precise Point Positioning Convergence with an Incremental Graph Optimizer*, 2018 IEEE/ION Position, Location and Navigation Symposium (PLANS), Monterey, CA, 2018; Monterey, CA, 2018; pp 589-596.
35. Zhang, G.; Ng, H.-F.; Wen, W.; Hsu, L.-T., 3D Mapping Database Aided GNSS Based Collaborative Positioning Using Factor Graph Optimization. *IEEE Transactions on Intelligent Transportation Systems* **2021,** 22, (10), 6175-6187.
36. Department of City Planning NYC 3D Model by Community District. https://www1.nyc.gov/site/planning/data-maps/open-data/dwn-nyc-3d-model-download.page
37. Robert McNeel Rhinoceros. https://www.rhino3d.com/
38. Epic Games Unreal Engine. https://www.unrealengine.com/en-US
39. van Diggelen, F., A-GPS; assisted GPS, GNSS, and SBAS. In Artech House Portland, 2009; Vol. 33.
40. van Diggelen, F., Assisted GNSS. In *Position, Navigation, and Timing Technologies in the 21st Century*, 2020; pp 419-444.
41. Groves, P. D., Shadow Matching: A New GNSS Positioning Technique for Urban Canyons. *Journal of Navigation* **2011,** 64, (3), 417-430.
42. Li, W.; Cui, X.; Lu, M., A robust graph optimization realization of tightly coupled GNSS/INS integrated navigation system for urban vehicles. *Tsinghua Science and Technology* **2018,** 23, (6), 724-732.
43. Takasu, T. In *RTKLIB: Open Source Program Package for RTK-GPS*, FOSS4G 2009 Tokyo, Japan, 2009; Japan, 2009.
44. Agarwal, S.; Mierle, K., Ceres solver: Tutorial & reference. *Google Inc.* **2012,** 2, (72), 8.
45. Hsu, L.-T.; Kubo, N.; Wen, W.; Chen, W.; Liu, Z.; Suzuki, T.; Meguro, J. In *UrbanNav:An Open-Sourced Multisensory Dataset for Benchmarking Positioning Algorithms Designed for Urban Areas*, Proceedings of the 34th International Technical Meeting of the Satellite Division of The Institute of Navigation (ION GNSS+ 2021), St. Louis, Missouri, 2021; St. Louis, Missouri, 2021; pp 226-256.
46. Suzuki, T.; Matsuo, K.; Amano, Y., Rotating GNSS Antennas: Simultaneous LOS and NLOS Multipath Mitigation. *GPS Solutions* **2020,** 24, (3), 86.
47. Xu, B.; Jia, Q.; Luo, Y.; Hsu, L. T., Intelligent GPS L1 LOS/multipath/NLOS classifiers based on correlator-, RINEX- and NMEA-level measurements. *Remote Sensing* **2019,** 11, (16), 1851.
48. Xie, P.; Petovello, M. G., Measuring GNSS Multipath Distributions in Urban Canyon Environments. *IEEE Transactions on Instrumentation and Measurement* **2015,** 64, (2), 366-377.